

# Structure of $\text{Mo}_2\text{C}_x$ and $\text{Mo}_4\text{C}_x$ Molybdenum Carbide Nanoparticles and Their Anchoring Sites on ZSM-5 Zeolites

Jie Gao,<sup>†</sup> Yiteng Zheng,<sup>†</sup> George B. Fitzgerald,<sup>\*,‡</sup> Jason de Joannis,<sup>‡</sup> Yadan Tang,<sup>§</sup> Israel E. Wachs,<sup>\*,§</sup> and Simon G. Podkolzin<sup>\*,†</sup>

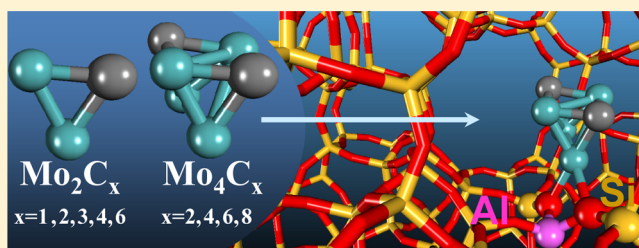
<sup>†</sup>Department of Chemical Engineering and Materials Science, Stevens Institute of Technology, Hoboken, New Jersey 07030, United States

<sup>‡</sup>Accelrys Software, Inc., San Diego, California 92121, United States

<sup>§</sup>Operando Molecular Spectroscopy & Catalysis Laboratory, Department of Chemical Engineering, Lehigh University, Bethlehem, Pennsylvania 18015, United States

## S Supporting Information

**ABSTRACT:** Mo carbide nanoparticles supported on ZSM-5 zeolites are promising catalysts for methane dehydroaromatization. For this and other applications, it is important to identify the structure and anchoring sites of Mo carbide nanoparticles. In this work, structures of  $\text{Mo}_2\text{C}_x$  ( $x = 1, 2, 3, 4,$  and  $6$ ) and  $\text{Mo}_4\text{C}_x$  ( $x = 2, 4, 6,$  and  $8$ ) nanoparticles are identified using a genetic algorithm with density functional theory (DFT) calculations. The ZSM-5 anchoring sites are determined by evaluating infrared vibrational spectra for surface OH groups before and after Mo deposition. The spectroscopic results demonstrate that initial Mo oxide species preferentially anchors on framework Al sites and partially on Si sites on the external surface of the zeolite. In addition, Mo oxide deposition causes some dealumination, and a small fraction of Mo oxide species anchor on extraframework Al sites. Anchoring modes of Mo carbide nanoparticles are evaluated with DFT cluster calculations and with hybrid quantum mechanical and molecular mechanical (QM/MM) periodic structure calculations. Calculation results suggest that binding through two Mo atoms is energetically preferable for all Mo carbide nanoparticles on double Al-atom framework sites and external Si sites. On single Al-atom framework sites, the preferential binding mode depends on the particle composition. The calculations also suggest that Mo carbide nanoparticles with a C/Mo ratio greater than 1.5 are more stable on external Si sites and, thus, likely to migrate from zeolite pores onto the external surface of the zeolite. Therefore, in order to minimize such migration, the C/Mo ratio for zeolite-supported Mo carbide nanoparticles under hydrocarbon reaction conditions should be maintained below 1.5.



## 1. INTRODUCTION

Supported Mo carbide nanoparticles are studied in multiple and diverse catalytic applications. For example, Mo carbide nanoparticles supported on  $\text{Al}_2\text{O}_3$  or  $\text{MgO}$  are active in Fischer–Tropsch synthesis,<sup>1–3</sup> bio-oil upgrading,<sup>4</sup> and methane conversion to synthesis gas with reforming or partial oxidation.<sup>5</sup> Mo carbide nanoparticles supported on carbon nanotubes and carbon black can serve as electrocatalysts for hydrogen production,<sup>6</sup> and those supported on  $\text{SiO}_2$  can catalyze ethane and propane dehydrogenation to olefins.<sup>7,8</sup> In addition, unsupported Mo carbide nanoparticles can catalyze hydrocarbon dehydrogenation with selectivity and activity comparable to those of supported Pt catalysts.<sup>9</sup> The structure of Mo carbide nanoparticles, however, is not well understood. Carbide nanoparticles with 10–23 Mo atoms created by laser ablation had a  $\text{Mo}_x\text{C}_{x+3}$  stoichiometry, while larger ones had a stoichiometry closer to  $\text{Mo}_x\text{C}_{x+2}$ , indicative of near cubic nanocrystallite structures.<sup>10</sup> Nanoparticles with  $\text{Mo}_8\text{C}_{12}$  and  $\text{Mo}_{14}\text{C}_{13}$  compositions were found to be particularly stable.<sup>10,11</sup> Cluster anions with a stoichiometry of  $\text{Mo}_x\text{C}_{4x}$  ( $x = 2–4$ )

produced from  $\text{Mo}(\text{CO})_6$  by laser radiation were found to be unreactive with  $\text{NH}_3$ ,  $\text{H}_2\text{O}$ , and  $\text{O}_2$ , suggesting that Mo atoms in these structures are unavailable for coordination.<sup>12</sup> The structure of a  $\text{Mo}_4\text{C}_2$  nanoparticle was identified with density functional theory (DFT) calculations and used for modeling catalytic conversion of  $\text{CO}_2$  to  $\text{CO}$  in the presence of  $\text{H}_2$ .<sup>13</sup>

Mo carbide nanoparticles supported on zeolites, especially on ZSM-5, are actively studied as catalysts for methane dehydroaromatization with the main reaction of methane conversion to benzene:  $6\text{CH}_4 = \text{C}_6\text{H}_6 + 9\text{H}_2$ . Mo is usually deposited on ZSM-5 either by an aqueous impregnation or by physically mixing  $\text{MoO}_3$  and a zeolite support with subsequent distribution of Mo species in the presence of gas-phase  $\text{O}_2$  at 700–1000 K. Both preparation methods yield similar catalysts.<sup>14–16</sup> Our studies<sup>17</sup> with ultraviolet–visible diffuse reflectance spectroscopy (UV–vis DRS), *operando* Raman

Received: October 27, 2013

Revised: February 11, 2014

Published: February 12, 2014

spectroscopy with simultaneous online mass spectrometry, infrared (IR) spectroscopy, and DFT calculations determined the identity of the initial Mo oxide structures as isolated  $\text{MoO}_2^{2+}$  species anchored on double Al-atom framework sites,  $2[\text{AlO}_4]^-$ , and  $\text{MoO}_2\text{OH}^+$  species anchored on single Al-atom framework sites,  $[\text{AlO}_4]^-$ . During an induction period under reaction conditions in methane flow, the initial Mo dioxo species are converted to oxycarbide ( $\text{MoO}_x\text{C}_y$ ) or carbide ( $\text{MoC}_x$ ) nanoparticles, which then catalyze methane conversion to benzene.<sup>17–26</sup> Moreover, Mo carbide nanoparticles, which are specially prepared without residual oxygen, supported on ZSM-5 are also active in methane dehydroaromatization.<sup>27</sup>

In addition to carburization, the initial atomically dispersed Mo oxide species agglomerate under methane dehydroaromatization reaction conditions. Images obtained with high-resolution transmission electron microscopy (HRTEM) show 2–15 nm Mo carbide nanoparticles on the external surface and particles with a size of less than 1 nm inside the ZSM-5 framework.<sup>20,28</sup> X-ray absorption (XAS), X-ray absorption near-edge structure (XANES), and extended X-ray absorption fine structure (EXAFS) spectra indicate the presence of 0.6–1 nm  $\text{MoC}_x$  particles with  $\sim 10$  Mo atoms.<sup>22,23</sup> Anchoring sites of Mo species in ZSM-5 were previously evaluated using titration with dimethyl ether<sup>18</sup> and  $^1\text{H}$  magic angle spinning nuclear magnetic resonance ( $^1\text{H}$  MAS NMR) measurements.<sup>19</sup>

For evaluation of structure–activity relationships for supported and unsupported Mo carbide nanoparticles in diverse catalytic and other applications as a function of their particle size and composition, structures of these nanoparticles with a variable number of Mo atoms and C/Mo ratios need to be determined. In this work, DFT calculations were used to identify structures of  $\text{Mo}_2\text{C}_x$  ( $x = 1, 2, 3, 4,$  and  $6$ ) and  $\text{Mo}_4\text{C}_x$  ( $x = 2, 4, 6,$  and  $8$ ) nanoparticles. For mechanistic studies of Mo/ZSM-5 catalysts in methane dehydroaromatization, it is also important to determine ZSM-5 anchoring sites and modes of binding of Mo carbide nanoparticles to these sites. In this work, *in situ* IR spectroscopic measurements were used to characterize ZSM-5 anchoring sites by comparing spectra of surface OH groups before and after Mo deposition for catalysts with a variable Si/Al ratio at a constant Mo loading and at a constant Si/Al ratio with a variable Mo loading. The IR results show that Mo oxide species primarily anchor on framework Al sites and partially on Si sites on the external surface of the zeolite. Since previous studies<sup>23</sup> demonstrated that the anchoring sites remain substantially the same after conversion of Mo oxide species into carbide nanoparticles, binding modes of  $\text{Mo}_2\text{C}_x$  and  $\text{Mo}_4\text{C}_x$  nanoparticles were evaluated with DFT calculations on three types of ZSM-5 anchoring sites: (1) single and (2) double Al-atom framework sites and (3) Si sites on the external surface. DFT calculations used a cluster model of a 10-member ZSM-5 pore as well as the same cluster imbedded into the full periodic structure of ZSM-5 using a hybrid method that combines quantum mechanical and molecular mechanical (QM/MM) calculations. The calculations compared the binding of  $\text{Mo}_2\text{C}_x$  and  $\text{Mo}_4\text{C}_x$  nanoparticles through 1 and 2 Mo atoms on all three evaluated ZSM-5 anchoring sites. In addition, the calculations compared thermodynamic stability of the Mo carbide nanoparticles on Al anchoring sites inside zeolite channels and Si sites on the external surface.

## 2. EXPERIMENTAL AND COMPUTATIONAL METHODS

**a. Catalyst Synthesis.** Two sets of Mo/ZSM-5 catalysts were prepared by incipient wetness impregnation using

aqueous Mo heptamolybdate  $(\text{NH}_4)_6\text{Mo}_7\text{O}_{24}\cdot 4\text{H}_2\text{O}$  (Alpha Aesar, 99.9%) and ZSM-5 zeolites (Zeolyst International). In the first catalyst set, the Mo loading was varied between 0.7 and 3.3 wt % using a ZSM-5 support with the Si/Al atomic ratio of 15 (Si/Al = 15, Zeolyst CBV 3024E). In the second catalyst set, the Mo loading was kept constant at 1.3 wt % for ZSM-5 supports with different Si/Al ratios: 15 (Zeolyst CBV 3024E), 25 (Zeolyst CBV 5524G), 40 (Zeolyst CBV 8014), and 140 (Zeolyst CBV 28014). After impregnation, the catalysts were dried at room temperature in air overnight and then by ramping to 393 K at 1 K/min and holding at this temperature for 5 h. After drying, the samples were calcined in flowing air (Airgas, Inc., ultrahigh purity) by ramping to 773 K at 1 K/min and holding at this temperature for 2 h.

**b. In Situ Infrared Spectroscopy.** IR measurements were performed with a Thermo Scientific Nicolet 8700 Research FTIR spectrometer equipped with a liquid nitrogen cooled mercury–cadmium telluride (MCT) detector, a Harrick Praying Mantis accessory (model DRA-2), and a Harrick reaction chamber HT-100. Catalyst samples were initially dehydrated in the Harrick cell under flowing 10 mol %  $\text{O}_2/\text{Ar}$  (Airgas, Inc., 10.00% Certified Mixture) at 723 K for 60 min and then cooled down to 383 K also under flowing 10 mol %  $\text{O}_2/\text{Ar}$ .

**c. Computational Methods.** Gradient-corrected spin-polarized periodic density functional theory (DFT) calculations were performed with the DMol<sup>3</sup> code in Materials Studio 6.1 program by Accelrys Software, Inc. The calculations used the DNP basis set (version 3.5) and the GGA RPBE functional. Tightly bound core electrons of Mo atoms were represented with semicore pseudopotentials. Reciprocal-space integration over the Brillouin zone was approximated through  $\Gamma$ -point sampling ( $1 \times 1 \times 1$  Monkhorst–Pack grid). The density mixing fraction of 0.2 with direct inversion in the iterative subspace (DIIS, size 6) and orbital occupancy with smearing of 0.005 Ha were used. The orbital cutoff distance was set at 0.44 nm for all atoms.

Optimized structures of Mo carbide nanoparticles shown in Figure 1 were obtained with a genetic algorithm using DFT

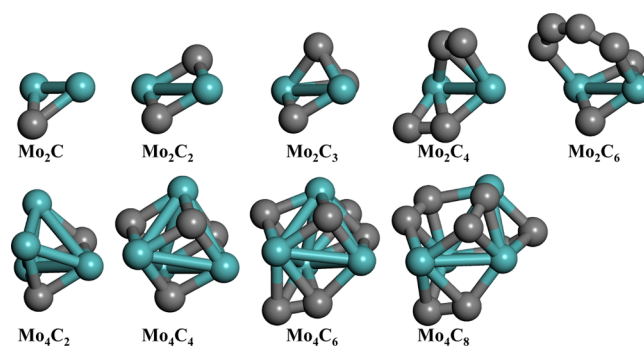


**Figure 1.** Structures of  $\text{Mo}_2\text{C}_x$  and  $\text{Mo}_4\text{C}_x$  nanoparticles identified with a genetic algorithm using DFT geometry optimization calculations.

geometry optimization calculations. The ZSM-5 structure was modeled with two approaches. In the first approach, a 10-T cluster (10 Si and 30 O atoms) was used with DFT calculations. In the second approach, the same 10-T cluster embedded into the full periodic MFI structure was used with QM/MM calculations. Both models are shown in Figure 2. The cluster was generated from a 10-T ring of the sinusoidal

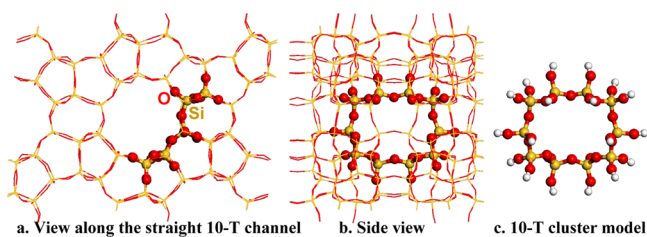


**Figure 2.** ZSM-5 computational models: (a) front and (b) side views of the periodic structure model constructed as a supercell from 2 MFI unit cells and used in QM/MM calculations. The 10-T region (shown as a ball and stick) was evaluated with QM and the rest of the structure (shown as a wire frame) with MM. (c) The same 10-T region as a cluster model for DFT calculations.

channel of an MFI unit cell (96 Si and 192 O atoms) with the experimental lattice constants of  $a = 2.0022$ ,  $b = 1.9899$ , and  $c = 1.3383$  nm. The dangling bonds of the boundary O atoms in the cluster were saturated by H atoms, as shown in Figure 2c. In order to minimize cluster boundary effects and better simulate the overall zeolite structure, the coordinates of these terminal OH groups were constrained. The terminal O atoms were constrained at their original positions in the MFI unit cell. The terminal H atoms were constrained at the positions obtained with the following two-step procedure. First, the bonding Si atoms from the part of the zeolite framework that was cut out from the cluster were changed into H atoms. Second, the distance between the bonding O atoms in the cluster and the terminal H atoms was adjusted to 0.095 nm. Except for the terminal OH groups, the positions of all other cluster atoms and all atoms in an anchored Mo carbide particle were optimized with DFT calculations.

In the second approach, the same 10-T cluster was selected in the middle of two full MFI unit cells ( $96 \times 2 = 192$  Si and  $192 \times 2 = 384$  O atoms) shown in Figures 2a,b, which were combined into a periodic supercell. The 10-T cluster and the boundary O atoms, which are shown in Figures 2a,b with a ball and stick representation, were treated as the DFT (QM) region, and the rest of the MFI supercell, which is shown in Figures 2a,b with a wire frame representation, was treated as the MM region. The QM region was embedded using mechanical embedding, with the total energy being calculated with a subtractive scheme. The QM/MM calculations used the same DFT settings as those employed in cluster calculations performed with DFT only. The MM calculations were performed with the GULP program using the Broyden–Fletcher–Goldfarb–Shanno (BFGS) optimization method and the universal force field (UFF).

A single Al-atom framework anchoring site was modeled by placing an Al atom into the T-9 framework position in the 10-T ring. This site is shown with an anchored  $\text{Mo}_2\text{C}_3$  particle in Figures 3a,b. A single Al atom in a zeolite framework has a counterion, for example  $\text{H}^+$ , that balances the charge of the corresponding  $[\text{AlO}_4]^-$  group. Therefore, although an Al atom has an odd number of electrons, the  $[\text{AlO}_4]^- \text{H}^+$  group has an even number of electrons. In order to maintain an even number of electrons in the DFT cluster with the single Al-atom site, an H atom was added to the models with this anchoring site. For anchored Mo carbides, the additional H atom was found to preferentially bind to a C atom. The position of the bonding C atom for each Mo carbide particle is labeled as C(1) in Figure S1. A double Al-atom framework anchoring site was modeled by placing one Al atom into the T-5 framework position and

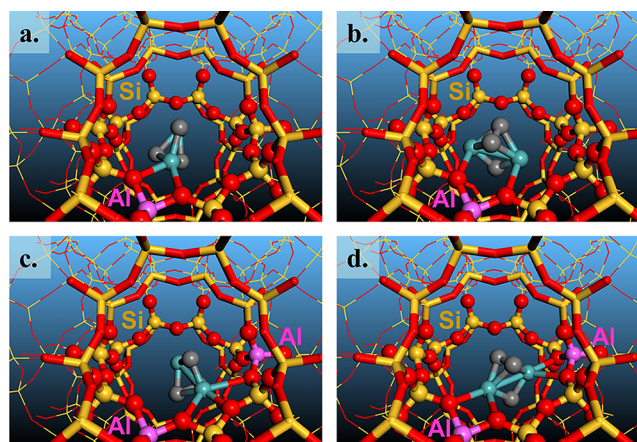


**Figure 3.** Anchoring modes for the  $\text{Mo}_2\text{C}_3$  nanoparticle on ZSM-5 framework Al sites: (a) single Al-atom site with binding through 1 Mo atom, (b) single Al-atom site with binding through 2 Mo atoms, (c) double Al-atom site with binding through 1 Mo atom, and (d) double Al-atom site with binding through 2 Mo atoms.

another Al atom into the T-9 position in the 10-T ring. This site is shown with an anchored  $\text{Mo}_2\text{C}_3$  particle in Figures 3c,d.

For comparison of double Al-atom framework sites and external Si sites, terminal H atoms from two neighboring Si sites in the T-1 and T-10 framework positions were moved to the T-5 and T-9 Al framework sites in the 10-T ring. The positions of these 2 H atoms were optimized as  $\text{H}^+$  Bronsted acids on the two  $[\text{AlO}_4]^-$  sites, as shown in Figures 6 and 8. The positions of the boundary O atoms on the T-1 and T-10 Si sites without terminal H atoms were relaxed and optimized with Mo carbide particles, simulating Si anchoring sites on the external surface of the zeolite. Since the stoichiometry of the 10-T cluster remained the same after the transfer of the 2 H atoms from the Si to Al sites, the energies of Mo carbides anchored on these two sites could be directly compared.

### 3. RESULTS

#### a. Structure of $\text{Mo}_2\text{C}_x$ and $\text{Mo}_4\text{C}_x$ Nanoparticles.

Optimized geometries of  $\text{Mo}_2\text{C}_x$  ( $x = 1, 2, 3, 4$ , and 6) and  $\text{Mo}_4\text{C}_x$  ( $x = 2, 4, 6$ , and 8) nanoparticles are shown in Figure 1. Geometry details (bond distances and angles) are provided in Tables S1–S9, and the atom numbering used in the geometry description is provided in Figure S1. Because of a large number of possible structures, minimum-energy structures were identified with a genetic algorithm based on the approach of Deaven and Ho.<sup>29</sup> For a given Mo carbide composition, multiple structures were generated and analyzed in order to identify the one with the lowest energy. The evaluation methodology was based on an adaptation of the principle of Darwinian evolution, in which the more fit individuals are more likely to pass their characteristics to future generations.<sup>30</sup> First, a population of 32 candidate structures was generated for a fixed Mo carbide composition and evaluated with DFT geometry optimization calculations. Then, a new generation of 32 “child” structures was created by combining portions of the initial “parent” population. The “parent” structures were selected on the basis of their fitness, which in this case was their total DFT energy. As a result, lower-energy structures were more likely to be selected to pass their characteristics to future generations. New “child” population structures were created with two methods: mutation and mating (also known as

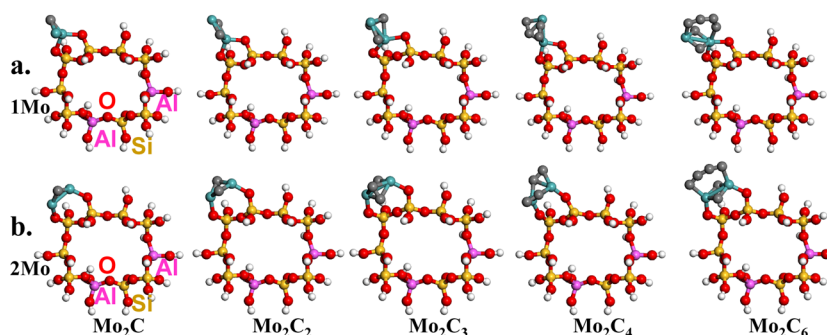


**Figure 6.** Anchoring modes for  $\text{Mo}_2\text{C}_x$  nanoparticles on Si sites on the external surface of ZSM-5: (a) binding through 1 Mo atom; (b) binding through 2 Mo atoms.

crossover). In the mutation method, Cartesian coordinates of an atom ( $x$ ,  $y$ , and  $z$ ) were modified randomly with a preset probability of 10%. In the mating method, two “parent” structures were selected to create two new “child” structures. A random plane passing through the center of mass of each “parent” structure was generated, and “child” structures were generated by selecting the atoms above the plane in one of the “parents” and below the plane in the other. In addition, a half of each “child” cluster was rotated through a random angle. Furthermore, seven variant crossover operations<sup>31</sup> were used to generate additional “child” population structures. For each pair of parents, a crossover operator was chosen randomly, ensuring a diverse population. Moreover, a “taboo” algorithm was employed that prevented generation of the same “child” structures in two consecutive generations, which further ensured the diversity of the population.

After generation of a complete set of 32 “child” structures, the fitness of each new structure was computed, and a subsequent population of 32 “child” structures was created. The process continued until convergence was achieved. Evaluation of populations larger than 32 structures for several Mo carbide compositions showed no significant improvements in convergence. The probability of selecting a “parent” structure was proportional to its relative energy. During the first few generations, however, high-energy clusters were assigned a higher probability than would be determined by their energy. This prevented the algorithm from converging to a local minimum. The likelihood of premature convergence was further minimized by employing a sliding scale factor for crossover probabilities.<sup>32</sup> The convergence criterion was set as an energy change of less than  $10^{-4}$  Ha (0.26255 kJ/mol) for 25 consecutive generations. We note that although it is possible to optimize structures with a genetic algorithm using single-point energy rather than geometry optimization calculations, the former method is typically slower.<sup>33</sup>

A histogram for the number of  $\text{Mo}_2\text{C}_6$  structures in a population as a function of their stability relative to the most stable structure for the  $\text{Mo}_2\text{C}_6$  stoichiometry is shown in Figure S2. The  $\text{Mo}_2\text{C}_6$  structure that has the second best geometry (shown as structure 2 in Figure S3) is substantially, by 70 kJ/mol, less stable than the most stable structure (shown in Figure 1 and also shown for comparison in Figure S3 as structure 1). A total of 3 structures are less stable relative to the most stable structure by 70–99 kJ/mol. The next 10 structures are relatively less stable by 100–199 kJ/mol (group 2), the next 12 structures are less stable by 200–299 kJ/mol (group 3), the next 11 structures are less stable by 300–499 kJ/mol (group 4), and, finally, the least stable 7 structures are less stable by 500–

1000 kJ/mol. Such a histogram is typical for the evaluated Mo carbide particles.

All optimized (lowest-energy) structures of  $\text{Mo}_2\text{C}_x$  particles, which are shown in Figure 1, maintain a Mo–Mo bond. The Mo–Mo bond distance increases from 0.21 nm in  $\text{Mo}_2\text{C}$  to 0.25–0.27 nm in the particles with a larger number of C atoms. All optimized structures of  $\text{Mo}_4\text{C}_x$  particles, which are also shown in Figure 1, maintain bonds among all 4 Mo atoms with similar bond distances of 0.23–0.29 nm. Distances for Mo–C bonds for both  $\text{Mo}_2\text{C}_x$  and  $\text{Mo}_4\text{C}_x$  particles are 0.19–0.23 nm. C atoms are located in bridging positions between Mo atoms. With the increasing number of C atoms, chains of C atoms that bridge 2 Mo atoms are formed. Initially, these bridging chains have 2 C atoms, as in  $\text{Mo}_2\text{C}_4$ ,  $\text{Mo}_4\text{C}_6$ , and  $\text{Mo}_4\text{C}_8$ . At a higher C/Mo ratio of 3 in the  $\text{Mo}_2\text{C}_6$  particle, the chain length increases to 4 C atoms. All C–C bond distances are 0.13–0.14 nm and consistent with the C=C double bond distance of 0.133 nm in gas-phase ethylene.

**b. Identification of Initial Mo Anchoring Sites with *In Situ* Infrared Spectroscopy.** Initial Mo oxide species anchor on the zeolite surface by replacing H atoms of surface OH groups. The IR spectra in Figure 4 with characteristic peaks for vibrations of surface OH groups provide information on anchoring sites based on changes in the intensities of these peaks after Mo oxide deposition. Importantly, previous studies<sup>23</sup> demonstrated that the anchoring sites for Mo oxide species are not fully recovered after the conversion of the initial oxide phase into Mo carbide nanoparticles. Therefore, the anchoring sites for Mo oxide species also serve as anchoring sites for Mo carbide nanoparticles.

Figure 4a shows an evolution of spectra in the OH vibrational region with the increasing Mo loading for the ZSM-5 support with the Si/Al ratio of 15. Figure 4b shows pairs of spectra before and after 1.3 wt % Mo deposition for ZSM-5 supports with the Si/Al ratios from 15 to 140 in the same OH vibrational region. The spectra for blank H-ZSM-5 (Si/Al = 15) and 1.3 wt % Mo on the same zeolite are shown in both sets for comparison. Most spectra exhibit four OH vibrational peaks at 3783, 3741, 3660, and 3608  $\text{cm}^{-1}$  assigned<sup>34,35</sup> respectively to type I extra-framework Al sites (ex-AIOH I), Si sites on the external zeolite surface (Si–OH), type II extra-framework Al sites (ex-AIOH II), and framework Al sites (Al–(OH)–Si).

The full spectrum for H-ZSM-5 (Si/Al = 15) prior to Mo deposition shown in Figure 4e exhibits a prominent peak at 1380  $\text{cm}^{-1}$  from Si–O–Si vibrations of the zeolite framework. Since Si–O–Si framework vibrations should be practically unaffected by Mo deposition, the peak at 1380  $\text{cm}^{-1}$  can serve

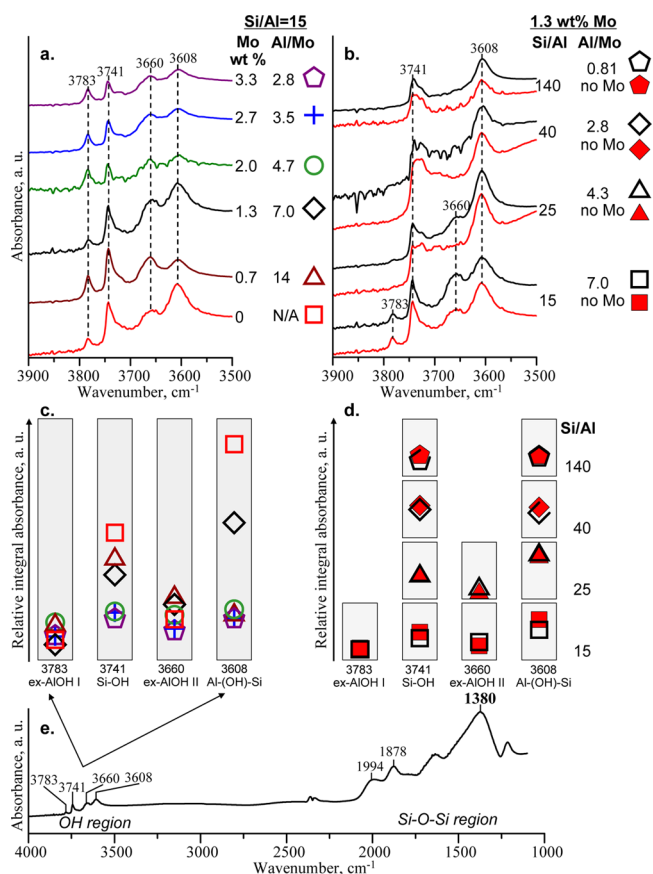


**Figure 4.** Comparison of IR spectra in the OH vibrational region for ZSM-5 before and after Mo deposition: (a) as a function of the Mo loading; (b) pairs of spectra as a function of the Si/Al ratio. Comparison of relative integral absorbance values for (c) spectra in part a and (d) spectra in part b. (e) Full spectrum for H-ZSM-5 (Si/Al = 15) before Mo deposition.

as a reference. Accordingly, the integral absorbance values for the four OH vibrational peaks in Figures 4a,b were normalized by dividing by the integral absorbance for the peak at 1380  $\text{cm}^{-1}$  in each spectrum, and the results are presented in Figures 4c,d.

At low Mo loadings, the intensity of the band at 3608  $\text{cm}^{-1}$  due to vibrations of hydroxyls on framework Al sites, Al-(OH)-Si, is reduced, indicating that Mo oxide species preferentially anchor on these sites. At higher Mo loadings, the intensity of the band at 3741  $\text{cm}^{-1}$  for hydroxyls on external Si sites, Si-OH, is reduced, indicating that external Si sites can serve as additional anchoring sites. Finally, the bands at 3660 and 3783  $\text{cm}^{-1}$  for hydroxyls on extra-framework Al sites, ex-AlOH, are perturbed, indicating that these Al sites can also serve as anchoring sites for a small fraction of Mo species. A similar trend is observed as a function of the Si/Al ratio. Additionally, as the Si/Al ratio increases and fewer Al sites are available, a higher fraction of external Si sites becomes occupied. Furthermore, Mo deposition causes some dealumination that is evidenced by changes in the peaks at 3660 and 3783  $\text{cm}^{-1}$ . If Mo species were only anchoring on existing extra-framework Al sites, then the intensities of these peaks should always decrease after Mo deposition. The slight increases in peak intensities observed for several catalysts indicate that Mo deposition causes the formation of additional extra-framework Al sites, which is not offset by anchoring of Mo species. This

dealumination effect caused by Mo deposition is consistent with reported  $^{27}\text{Al}$  MAS NMR and  $\text{NH}_3$  titration measurements.<sup>36</sup>

**c. Anchoring of Mo Carbide Nanoparticles.** Anchoring of  $\text{Mo}_2\text{C}_x$  and  $\text{Mo}_4\text{C}_x$  nanoparticles was evaluated computationally on three types of sites: (1) single and (2) double Al-atom framework sites and (3) Si sites on the external surface. On all sites, binding through 1 and 2 Mo atoms was compared. The structures with framework Al sites were first calculated using the 10-T cluster shown in Figure 2c and then recalculated with the periodic model shown in Figures 2a,b.

Results for the  $\text{Mo}_2\text{C}_x$  particles anchored on the single Al-atom site are presented in Table 1 and Figures 5a,b. Binding

**Table 1. Relative Stability of  $\text{Mo}_2\text{C}_x$  Nanoparticles Binding through 2 Mo Atoms vs 1 Mo Atom for the 10-T Cluster Model (and Full Periodic ZSM-5 Structure),  $\text{kJ/mol}^a$**

	$\Delta E$ , single Al-atom framework site	$\Delta E$ , Si site on external surface
$\text{Mo}_2\text{C}$	10 (3)	34
$\text{Mo}_2\text{C}_2$	26 (23)	52
$\text{Mo}_2\text{C}_3$	-96 (-79)	44
$\text{Mo}_2\text{C}_4$	11 (-23)	179
$\text{Mo}_2\text{C}_6$	-6 (-19)	204

<sup>a</sup>Positive numbers mean that binding through 2 Mo atoms is energetically preferable. Corresponding geometries are shown in Figures 5a,b and 6.

through 2 Mo atoms is energetically preferable for the  $\text{Mo}_2\text{C}$  and  $\text{Mo}_2\text{C}_2$  particles. For the  $\text{Mo}_2\text{C}_3$  particle, this trend is reversed, and binding through 1 Mo atom (Figures 3a and 5a) is preferable than through 2 Mo atoms (Figures 3b and 5b). With increasing C/Mo ratio, binding through 1 Mo atom remains favorable. The results of DFT cluster calculations and periodic QM/MM calculations in Table 1 are in general agreement, within 17  $\text{kJ/mol}$ . An exception is the  $\text{Mo}_2\text{C}_4$  particle with an energy difference of 34  $\text{kJ/mol}$ . These differences are due to a better description of relaxation effects in the zeolite framework around the anchoring site by the QM/MM periodic structure calculations compared to the DFT-only calculations with the rigid cluster. Binding through 1 Mo atom (Figure 5a) in general requires greater relaxation of the zeolite framework than through 2 Mo atoms (Figure 5b). As a result, periodic calculations in general predict greater stability for binding through 1 Mo atom and, therefore, lower values for the preferential binding through 2 Mo atoms in Table 1. An exception for this trend is the  $\text{Mo}_2\text{C}_3$  particle, which is particularly stable by binding through 1 Mo atom (Figure 3a). This is also the only Mo carbide particle that is stable by binding through 1 Mo atom on the double Al-atom site (Figure 3c). All other evaluated Mo carbide particles anchor on the double Al-atom site by binding only through 2 Mo atoms (Figure 5c). Even though the structure with binding through 1 Mo atom on the double Al-atom site is stable for the  $\text{Mo}_2\text{C}_3$  particle (Figure 3c), it is still less preferable by 129  $\text{kJ/mol}$  than that with binding through 2 Mo atoms (Figure 3d).

External Si sites offer greater flexibility in the positions of anchoring O atoms derived from surface OH groups compared to framework O atoms of Al sites. Therefore, in contrast to the double Al-atom framework site, configurations with binding through 1 Mo atom are stable on 2 Si atoms on the external surface (Figure 6a). Binding through 2 Mo atoms (Figure 6b), however, remains preferable for all  $\text{Mo}_2\text{C}_x$  particles, with the

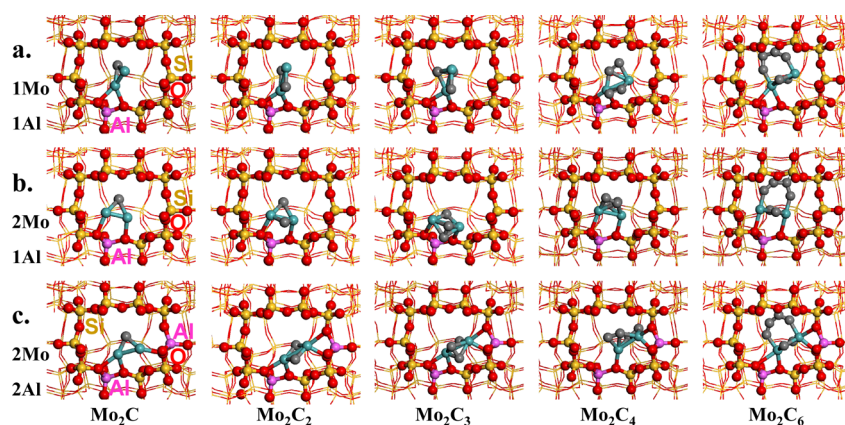


**Figure 5.** Anchoring modes for  $\text{Mo}_2\text{C}_x$  nanoparticles on ZSM-5 framework Al sites: (a) single Al-atom site with binding through 1 Mo atom, (b) single Al-atom site with binding through 2 Mo atoms, and (c) double Al-atom site with binding through 2 Mo atoms.

relative stability increasing with the C/Mo ratio from 34 kJ/mol for the  $\text{Mo}_2\text{C}$  particle to 204 kJ/mol for the  $\text{Mo}_2\text{C}_6$  particle (Table 1). A notable exception in this trend of gradually increasing relative stability values is, again, the  $\text{Mo}_2\text{C}_3$  particle with a lower value compared to the trend.

The relative stability values for the  $\text{Mo}_2\text{C}_x$  particles binding through 2 Mo atoms anchored on the double Al-atom framework site (Figure 5c) and external Si site (Figure 6b) are compared in Table 2. For Mo carbide particles with the C/

**Table 2. Relative Stability of  $\text{Mo}_2\text{C}_x$  Nanoparticles Anchored on Double Al-Atom Framework vs External Si Sites, kJ/mol<sup>a</sup>**

	$\Delta E$		$\Delta E$
$\text{Mo}_2\text{C}$	78	$\text{Mo}_2\text{C}_4$	-50
$\text{Mo}_2\text{C}_2$	68	$\text{Mo}_2\text{C}_6$	-32
$\text{Mo}_2\text{C}_3$	125		

<sup>a</sup>Positive numbers mean that anchoring on the double Al-atom framework site is energetically preferable. Corresponding geometries are shown in Figures 5c and 6b.

Mo ratio of 1.5 or lower ( $\text{Mo}_2\text{C}$ ,  $\text{Mo}_2\text{C}_2$ , and  $\text{Mo}_2\text{C}_3$ ), anchoring in a zeolite pore on the double Al-atom site is preferable. However, for particles with the C/Mo ratio of 2 and higher ( $\text{Mo}_2\text{C}_4$  and  $\text{Mo}_2\text{C}_6$ ), the relative stability is reversed and anchoring on the external Si site becomes energetically preferable. For the  $\text{Mo}_2\text{C}_3$  particle, an additional comparison is available between the configurations with binding through 1 Mo atom on the double Al-atom framework site (Figure 3c) and external Si site (Figure 6a). Anchoring on the double Al-atom framework site is preferable by 40 kJ/mol, which is in line with the preferential anchoring for this particle by binding through 2 Mo atoms in Table 2.

In order to confirm that the identified unanchored optimized Mo carbide structures in Figure 1 generate the most stable structures when they are anchored, additional calculations were performed to compare six different structures with the same  $\text{Mo}_2\text{C}_6$  stoichiometry when they are unanchored and anchored on the different types of ZSM-5 sites. In addition to the lowest-energy unanchored  $\text{Mo}_2\text{C}_6$  structure, which is shown in Figure 1 and as also in Figure S3 as structure 1, five more  $\text{Mo}_2\text{C}_6$  structures with the energies closest to best structure were evaluated. These additional  $\text{Mo}_2\text{C}_6$  structures are shown in Figure S3 as structures 2–6, and their geometries are provided in Tables S5.2–S5.6. The corresponding optimized structures

anchored on single Al-atom, double Al-atom, and external Si sites of the 10-T ZSM-5 cluster are shown in Figure S4, and their energies are summarized in Figure S5. Without anchoring, the additional five  $\text{Mo}_2\text{C}_6$  structures 2–6 are less stable than the lowest-energy structure 1 by 70–126 kJ/mol. When anchored on the ZSM-5 sites, only  $\text{Mo}_2\text{C}_6$  structure 2 on the Si site generates an alternative geometry that is comparable in energy to that obtained with the lowest-energy  $\text{Mo}_2\text{C}_6$  structure 1. The  $\text{Mo}_2\text{C}_6$  structure 5 optimizes to exactly the same geometries as those obtained with the lowest-energy  $\text{Mo}_2\text{C}_6$  structure 1 on double Al-atom and Si sites (energy difference of zero in Figure S5). All other anchored structures remain less stable by 54–233 kJ/mol. Therefore, Mo carbide structures, which are the most stable without anchoring, in general generate the most stable anchored structures.

Results for the  $\text{Mo}_4\text{C}_x$  particles anchored on the single Al-atom site are presented in Table 3 and Figures 7a,b. Preferential

**Table 3. Relative Stability of  $\text{Mo}_4\text{C}_x$  Nanoparticles Binding through 2 Mo Atoms vs 1 Mo Atom for the 10-T Cluster Model (and Full Periodic ZSM-5 Structure), kJ/mol<sup>a</sup>**

	$\Delta E$ , single Al-atom framework site	$\Delta E$ , Si site on external surface
$\text{Mo}_4\text{C}_2$	13 (3)	162
$\text{Mo}_4\text{C}_4$	-21 (n/a)	184
$\text{Mo}_4\text{C}_6$	-34 (-73)	148
$\text{Mo}_4\text{C}_8$	-6 (9)	150

<sup>a</sup>Positive numbers mean that binding through 2 Mo atoms is energetically preferable. Corresponding geometries are shown in Figures 7a,b and 8.

binding is through Mo atoms that have fewer bonded C atoms. Based on the periodic structure calculations, binding through 2 Mo atoms is preferable for the  $\text{Mo}_4\text{C}_2$  and  $\text{Mo}_4\text{C}_8$  particles. In contrast, binding through 1 Mo atom is preferable for the  $\text{Mo}_4\text{C}_4$  and  $\text{Mo}_4\text{C}_6$  particles. For the  $\text{Mo}_4\text{C}_4$  particle, the geometry with binding through 2 Mo atoms is not even stable in the periodic structure as it optimizes to the geometry with binding through 1 Mo atom (Figure 7a). Therefore, the anchored  $\text{Mo}_4\text{C}_4$  particle with binding through 1 Mo atom is shown in Figure 7b in the cluster model, not in the periodic structure.

Similarly to the  $\text{Mo}_2\text{C}_x$  particles anchored on the external Si site, binding through 2 Mo atoms (Figure 8b) is preferable by 148–184 kJ/mol compared to binding through 1 Mo atom

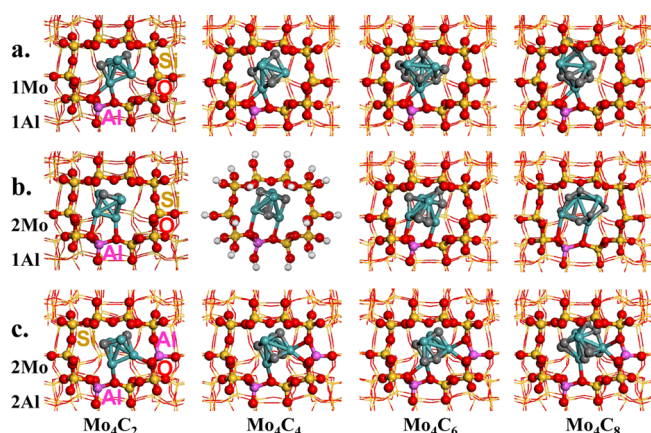


**Figure 7.** Anchoring modes for  $\text{Mo}_4\text{C}_x$  nanoparticles on ZSM-5 framework Al sites: (a) single Al-atom site with binding through 1 Mo atom, (b) single Al-atom site with binding through 2 Mo atoms, and (c) double Al-atom site with binding through 2 Mo atoms.

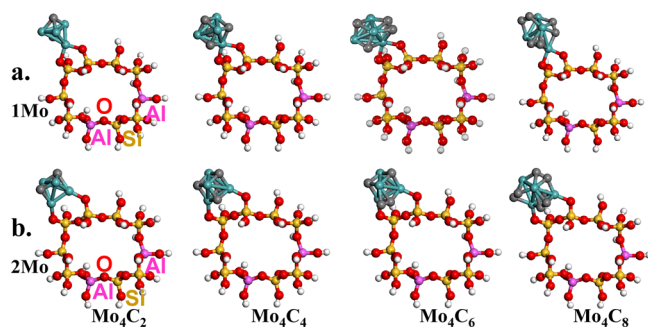


**Figure 8.** Anchoring modes for  $\text{Mo}_4\text{C}_x$  nanoparticles on Si sites on the external surface of ZSM-5: (a) binding through 1 Mo atom; (b) binding through 2 Mo atoms.

(Figure 8a) for all  $\text{Mo}_4\text{C}_x$  particles (Table 3). However, unlike for the  $\text{Mo}_2\text{C}_x$  particles, no trend is observed with the increasing C/Mo ratio.

The relative stability values for the  $\text{Mo}_4\text{C}_x$  particles binding through 2 Mo atoms anchored on the double Al-atom framework site (Figure 7c) and external Si site (Figure 8b) are compared in Table 4. For this comparison, the trend with

**Table 4. Relative Stability of  $\text{Mo}_4\text{C}_x$  Nanoparticles Anchored on Double Al-Atom Framework vs External Si Sites, kJ/mol<sup>a</sup>**

	$\Delta E$
$\text{Mo}_4\text{C}_2$	97
$\text{Mo}_4\text{C}_4$	77
$\text{Mo}_4\text{C}_6$	77
$\text{Mo}_4\text{C}_8$	-10

<sup>a</sup>Positive numbers mean that anchoring on the double Al-atom framework site is energetically preferable. Corresponding geometries are shown in Figures 7c and 8b.

the C/Mo ratio is the same as that for the  $\text{Mo}_2\text{C}_x$  particles: at the C/Mo ratio of 1.5 or lower ( $\text{Mo}_4\text{C}_2$ ,  $\text{Mo}_4\text{C}_4$ , and  $\text{Mo}_4\text{C}_6$ ), anchoring in a zeolite pore on the double Al-atom site is preferable. However, at the C/Mo ratio of 2 for the  $\text{Mo}_4\text{C}_8$  particle, the relative stability is reversed and anchoring on the external Si site becomes energetically preferable.

#### 4. DISCUSSION

The structure of the  $\text{Mo}_4\text{C}_2$  particle in Figure 1 is consistent with the geometry identified previously using DFT calculations and used for modeling catalytic reduction of  $\text{CO}_2$ .<sup>13</sup> Structures of other Mo carbide particles in Figure 1 are reported in this study for the first time.

These structures are useful for modeling catalytic reaction trends as a function of the particle size and composition because such characteristics are difficult to determine experimentally and because they are likely to change dynamically under reaction conditions. Mo carbide materials are usually prepared from an oxide phase by carburization, which is a complex process that depends on the initial phase and treatment conditions. For example, carburization of bulk orthorhombic  $\text{MoO}_3$  samples was monitored with X-ray diffraction (XRD) measurements and found to proceed through the formation of monoclinic  $\text{MoO}_2$  and cubic (fcc)  $\text{MoO}_x\text{C}_y$  structures before the conversion into a hexagonal (hcp)  $\beta\text{-MoC}_2$  phase.<sup>37</sup> For zeolite supports, multiple techniques show that the initial highly dispersed Mo oxide phase agglomerates and carburizes under reaction conditions with methane or another hydrocarbon. There is, however, uncertainty with respect to the structure of formed Mo carbide nanoparticles. For example, while XANES measurements for Mo/ZSM-5 after reaction with methane were interpreted in favor of  $\beta\text{-MoC}_2$ ,<sup>18</sup> electron paramagnetic resonance (EPR) spectra suggested that some particles remained partially oxidized in the form of oxycarbides  $\text{MoO}_x\text{C}_y$ .<sup>20,21</sup> In order to avoid the presence of residual oxygen, Mo carbide nanoparticles supported on ZSM-5 were prepared by carburization of  $\text{Mo}_2\text{N}$  and decarbonylation of  $\text{Mo}(\text{CO})_6$  and shown to be active in methane dehydroaromatization.<sup>27</sup> Moreover, for Mo/Al-FSM-16, formation of  $\alpha\text{-Mo}_2\text{C}_{1-x}$  and  $\eta\text{-Mo}_3\text{C}_2$  phases in addition to  $\beta\text{-Mo}_2\text{C}$  was identified by temperature-programmed desorption (TPD) and XRD measurements.<sup>38</sup> For unsupported Mo carbides used in methane reforming,  $\eta\text{-Mo}_3\text{C}_2$  was determined to be more catalytically active than both  $\alpha\text{-Mo}_2\text{C}_{1-x}$  and  $\beta\text{-Mo}_2\text{C}$  phases.<sup>39</sup>

The *in situ* IR results in Figure 4 show that the initial Mo oxide species anchor preferentially by displacing  $\text{H}^+$  on framework  $[\text{AlO}_4]^-$  sites. This result is in line with earlier measurements using dimethyl ether titration,<sup>18</sup>  $^1\text{H}$  MAS NMR,<sup>19</sup> and temperature-programmed oxidation.<sup>23</sup> Since  $\text{H}^+$  can serve as a counterion for only one framework  $[\text{AlO}_4]^-$  site, all OH groups on Al framework sites are similar with a single IR peak at  $3608\text{ cm}^{-1}$  in Figure 4. Similarly to  $\text{H}^+$ , cations with a charge of 1+, such as  $\text{MoO}_2\text{OH}^+$ , can serve as a counterion for one  $[\text{AlO}_4]^-$  framework site, i.e., a single framework Al-atom site.<sup>17</sup> In this case, each anchored Mo atom displaces 1 Brønsted acid site. However, in contrast to  $\text{H}^+$ , cations with a charge of 2+, such as  $\text{MoO}_2^{2+}$ , can serve as a counterion for 2 adjacent  $[\text{AlO}_4]^-$  sites, which become a double Al-atom anchoring site.<sup>17</sup> In this case, each anchored Mo atom displaces 2 Brønsted acid sites. Although the exact distribution of Al atoms among different framework sites in ZSM-5 is unknown, it can reportedly<sup>40</sup> be varied by adjusting the synthesis procedure. For example, the number of Al atoms serving as double Al-atom anchoring sites for hydrated Co cations can be varied from 4 to 46% of all Al atoms in ZSM-5 ( $\text{Si}/\text{Al} = \sim 20$ ).<sup>40</sup> The fraction of Al atoms that can serve as double Al-atom anchoring sites typically decreases more rapidly than the overall number of Al atoms with increasing Si/Al ratio. Our *in situ*

Raman spectroscopic results show that at 1.3 wt % Mo loading  $\text{MoO}_2^{2+}$  anchored on double Al-atom framework sites are the dominant initial oxide species for ZSM-5 with the Si/Al ratio of 15, and in contrast,  $\text{MoO}_2\text{OH}^+$  anchored on single Al-atom framework sites become the dominant species at a higher Si/Al ratio of 25.<sup>17</sup> These results are consistent with titration measurements that demonstrate that the number of  $\text{H}^+$  Brønsted acid sites displaced by each anchored Mo atom decreases from 2 to 1 when the ZSM-5 Si/Al ratio changes from 15 to 40.<sup>41</sup> Since ZSM-5 is a Si-rich zeolite, Lowenstein's rule applies, prohibiting Al atoms from being first neighbors in the framework as Al–O–Al. An arrangement of Al–O–Si–O–Al with two Al atoms as second neighbors was not found based on <sup>27</sup>Al NMR measurements and additional experimental characterization of ZSM-5 samples with Si/Al > 8.<sup>40,42</sup> Our computational evaluation of all framework T sites in a ZSM-5 unit cell shows that only special arrangements with 2 Al atoms as third neighbors, Al–O–(Si–O)<sub>2</sub>–Al, in T sites with a separation distance of less than 0.7 nm can serve as double Al-atom anchoring sites for  $\text{MoO}_2^{2+}$  species.<sup>17</sup> Since  $\text{Mo}_2\text{C}_x$  and  $\text{Mo}_4\text{C}_x$  particles are larger than the oxide species with a single Mo atom, a larger fraction of all Al atoms should be available as their double Al-atom anchoring sites.

The Si anchoring sites on the external surface of the zeolite were modeled in this study as OH groups on 2 neighboring Si atoms (Figures 6 and 8). This model accurately describes the structure and anchoring of isolated  $\text{MoO}_2$  species on such sites,<sup>17</sup> which are similar to those on the surface of amorphous  $\text{SiO}_2$ .<sup>43</sup> The  $\text{MoO}_2$  species anchored on external surface Si sites as (Si–O)<sub>2</sub>Mo(O)<sub>2</sub> were observed with *in situ* Raman spectroscopy at 1.3 wt % Mo loading for ZSM-5 (Si/Al = 140) when the Al/Mo ratio drops below unity and, therefore, when there are not enough Al framework sites for anchoring all Mo atoms.<sup>17</sup>

Previous studies with XRD, energy-dispersive X-ray spectroscopy (EDX), and differential thermal analysis (DTA) measurements showed that the C/Mo ratio gradually increases for Mo carbide nanoparticles supported on ZSM-5 under methane dehydroaromatization reaction conditions with time on stream and that the Mo carbide particles become eventually covered with graphite layers.<sup>28</sup> The relative stability values in Tables 2 and 4 show that it is energetically preferable for the Mo carbide particles with the C/Mo ratio of 1.5 or below to anchor on double Al-atom sites in zeolite pores rather than on Si sites on the external surface of the zeolite. In contrast, at higher C/Mo ratios, external Si sites become more preferable. Since zeolite-supported Mo species are known to agglomerate and, therefore, to be mobile under hydrocarbon reaction conditions, these results suggest that Mo carbide nanoparticles with the C/Mo ratio larger than 1.5 are likely to migrate out of zeolite pores onto the external surface of the zeolite. Consequently, such migration can potentially be minimized under reaction conditions by controlling the C/Mo ratio at values below 1.5 with, for example, gas-phase  $\text{O}_2$  or  $\text{H}_2$  treatments.

## 5. CONCLUSIONS

Structures of  $\text{Mo}_2\text{C}_x$  ( $x = 1, 2, 3, 4$ , and 6) and  $\text{Mo}_4\text{C}_x$  ( $x = 2, 4, 6$ , and 8) nanoparticles were identified using a genetic algorithm with DFT geometry optimization calculations. In all particles, Mo–Mo bonds are preserved with the increasing C/Mo ratio. The C atoms are initially incorporated as single atoms in bridging positions between 2 Mo atoms. Additional C

atoms are incorporated by forming bridging chains with 2 C atoms connected by double bonds that are similar to the C=C bond in ethylene. At a higher C/Mo ratio of 3 in the  $\text{Mo}_2\text{C}_6$  particle, the bridging chain length increases to 4 C atoms.

The ZSM-5 anchoring sites for Mo oxide species, which are also expected to be the anchoring sites for Mo carbide nanoparticles, were determined by evaluating changes in the vibrational peaks for surface OH groups after Mo oxide deposition with *in situ* IR spectroscopy as a function of the Mo loading at a constant Si/Al ratio and as a function of the Si/Al ratio at a constant Mo loading. The IR results demonstrate that Mo oxide species preferentially anchor on framework Al sites and partially on Si sites on the external surface of the zeolite. In addition, Mo deposition causes some dealumination of the zeolite framework, and a small fraction of Mo oxide species anchor on extraframework Al sites.

Anchoring of the Mo carbide nanoparticles on double and single Al-atom framework sites and on Si sites on the external surface of the zeolite was evaluated with DFT cluster calculations and QM/MM periodic structure calculations. Binding to the zeolite anchoring sites through Mo atoms with a fewer number of bonded C atoms is energetically preferable. Binding through 2 Mo atoms is energetically preferable for all Mo carbide particles on double Al-atom framework sites and external Si sites. On single Al-atom framework sites, the preferential binding mode depends on the particle composition. It is energetically preferable for the Mo carbide particles with the C/Mo ratio of 1.5 or below to anchor on double Al-atom sites in zeolite pores than on Si sites on the external surface of the zeolite. The Mo carbide particles with the C/Mo ratios greater than 1.5 preferentially anchor on external Si sites, which suggests that these particles would tend to migrate from zeolite pores onto the external surface of the zeolite. Therefore, in order to minimize such migration, the C/Mo ratio under hydrocarbon reaction conditions should be maintained below 1.5 with, for example, gas-phase  $\text{O}_2$  or  $\text{H}_2$  treatments.

## ■ ASSOCIATED CONTENT

### 📄 Supporting Information

Geometry details for  $\text{Mo}_2\text{C}_x$  and  $\text{Mo}_4\text{C}_x$  nanoparticles shown in Figure 1 are provided in Tables S1–S9, and the atom numbering used in the geometry description is provided in Figure S1; additional analysis of anchored and unanchored  $\text{Mo}_2\text{C}_6$  structures is provided in Figures S2–S5. This material is available free of charge via the Internet at <http://pubs.acs.org>.

## ■ AUTHOR INFORMATION

### Corresponding Authors

\*E-mail: [George.Fitzgerald@Accelrys.com](mailto:George.Fitzgerald@Accelrys.com) (G.B.F.).

\*E-mail: [iew0@Lehigh.edu](mailto:iew0@Lehigh.edu) (I.E.W.).

\*E-mail: [Simon.Podkolzin@Stevens.edu](mailto:Simon.Podkolzin@Stevens.edu) (S.G.P.).

### Notes

The authors declare no competing financial interest.

## ■ ACKNOWLEDGMENTS

The work in Israel E. Wach's group at Lehigh University was supported by the National Science Foundation under grant CBET-1134012. The work in Simon G. Podkolzin's group at Stevens Institute of Technology was supported by the National Science Foundation under grant CBET-1133987. Calculations

were performed with Materials Studio software provided by Accelrys Software, Inc., in San Diego, CA.

## REFERENCES

- (1) Shou, H.; Davis, R. J. Multi-Product Steady-State Isotopic Transient Kinetic Analysis of CO Hydrogenation over Supported Molybdenum Carbide. *J. Catal.* **2013**, *306*, 91–99.
- (2) Shou, H.; Davis, R. J. Reactivity and in Situ X-Ray Absorption Spectroscopy of Rb-Promoted Mo<sub>2</sub>C/MgO Catalysts for Higher Alcohol Synthesis. *J. Catal.* **2011**, *282*, 83–93.
- (3) Vo, D.-V. N.; Adesina, A. A. Fischer–Tropsch Synthesis over Alumina-Supported Molybdenum Carbide Catalyst. *Appl. Catal., A* **2011**, *399*, 221–232.
- (4) Patel, M. A.; Baldanza, M. A. S.; Teixeira da Silva, V.; Bridgwater, A. V. in Situ Catalytic Upgrading of Bio-Oil Using Supported Molybdenum Carbide. *Appl. Catal., A* **2013**, *458*, 48–54.
- (5) Claridge, J. B.; York, A. P. E.; Brungs, A. J.; Marquez-Alvarez, C.; Sloan, J.; Tsang, S. C.; Green, M. L. H. New Catalysts for the Conversion of Methane to Synthesis Gas: Molybdenum and Tungsten Carbide. *J. Catal.* **1998**, *180*, 85–100.
- (6) Chen, W.-F.; Wang, C.-H.; Sasaki, K.; Marinkovic, N.; Xu, W.; Muckerman, J. T.; Zhu, Y.; Adzic, R. R. Highly Active and Durable Nanostructured Molybdenum Carbide Electrocatalysts for Hydrogen Production. *Energy Environ. Sci.* **2013**, *6*, 943–951.
- (7) Solymosi, F.; Németh, R. The Oxidative Dehydrogenation of Ethane with CO<sub>2</sub> over Mo<sub>2</sub>C/SiO<sub>2</sub> Catalyst. *Catal. Lett.* **1999**, *62*, 197–200.
- (8) Solymosi, F.; Németh, R.; Óvári, L.; Egri, L. Reactions of Propane on Supported Mo<sub>2</sub>C Catalysts. *J. Catal.* **2000**, *195*, 316–325.
- (9) Hyeon, T.; Fang, M.; Suslick, K. S. Nanostructured Molybdenum Carbide: Sonochemical Synthesis and Catalytic Properties. *J. Am. Chem. Soc.* **1996**, *118*, 5492–5493.
- (10) Lightstone, J. M.; Mann, H. A.; Wu, M.; Johnson, P. M.; White, M. G. Gas-Phase Production of Molybdenum Carbide, Nitride, and Sulfide Clusters and Nanocrystallites. *J. Phys. Chem. B* **2003**, *107*, 10359–10366.
- (11) Duncan, M. A. Synthesis and Characterization of Metal–Carbide Clusters in the Gas Phase. *J. Cluster Sci.* **1997**, *8*, 239–266.
- (12) Jin, C.; Haufler, R. E.; Hettich, R. L.; Barshick, C. M.; Compton, R. N.; Puzos, A. A.; Dem'yanenko, A. V.; Tuinman, A. A. Synthesis and Characterization of Molybdenum Carbide Clusters Mo<sub>n</sub>C<sub>4n</sub> (n = 1 to 4). *Science* **1994**, *263*, 68–71.
- (13) Tominaga, H.; Nagai, M. Density Functional Study of Carbon Dioxide Hydrogenation on Molybdenum Carbide and Metal. *Appl. Catal., A* **2005**, *282*, 5–13.
- (14) Aboul-Gheit, A. K.; Awadallah, A. E. Effect of Combining the Metals of Group VI Supported on H-ZSM-5 Zeolite as Catalysts for Non-Oxidative Conversion of Natural Gas to Petrochemicals. *J. Nat. Gas Chem.* **2009**, *18*, 71–77.
- (15) Aboul-Gheit, A. K.; Awadallah, A. E.; El-Kossy, S. M.; Mahmoud, A.-L. H. Effect of Pd or Ir on the Catalytic Performance of Mo/H-ZSM-5 during the Non-Oxidative Conversion of Natural Gas to Petrochemicals. *J. Nat. Gas Chem.* **2008**, *17*, 337–343.
- (16) Liu, H.; Bao, X.; Xu, Y. Methane Dehydroaromatization under Nonoxidative Conditions over Mo/HZSM-5 Catalysts: Identification and Preparation of the Mo Active Species. *J. Catal.* **2006**, *239*, 441–450.
- (17) Gao, J.; Jehng, J.-M.; Tang, Y.; Wachs, I. E.; Podkolzin, S. G. Identification of Molybdenum Oxide Structures on ZSM-5 for Catalytic Conversion of Natural Gas to Liquids. Submitted 2014.
- (18) Bedard, J.; Hong, D.-Y.; Bhan, A. CH<sub>4</sub> Dehydroaromatization on Mo/H-ZSM-5: I. Effects of Co-Processing H<sub>2</sub> and CH<sub>3</sub>COOH. *J. Catal.* **2013**, *306*, 58–67.
- (19) Zheng, H.; Ma, D.; Bao, X.; Hu, J. Z.; Kwak, J. H.; Wang, Y.; Peden, C. H. F. Direct Observation of the Active Center for Methane Dehydroaromatization Using an Ultrahigh Field <sup>95</sup>Mo NMR Spectroscopy. *J. Am. Chem. Soc.* **2007**, *130*, 3722–3723.
- (20) Zaikovskii, V. I.; Vosmerikov, A. V.; Anufrienko, V. F.; Korobitsyna, L. L.; Kodenev, E. G.; Echevskii, G. V.; Vasenin, N. T.; Zhuravkov, S. P.; Matus, E. V.; Ismagilov, Z. R.; Parmon, V. N. Properties and Deactivation of the Active Sites of an MoZSM-5 Catalyst for Methane Dehydroaromatization: Electron Microscopic and EPR Studies. *Kinet. Catal.* **2006**, *47*, 389–394.
- (21) Liu, H.; Shen, W.; Bao, X.; Xu, Y. Identification of Mo Active Species for Methane Dehydro-Aromatization over Mo/HZSM-5 Catalysts in the Absence of Oxygen: <sup>1</sup>H MAS NMR and EPR Investigations. *J. Mol. Catal. A: Chem.* **2006**, *244*, 229–236.
- (22) Lacheen, H. S.; Iglesia, E. Stability, Structure, and Oxidation State of Mo/H-ZSM-5 Catalysts during Reactions of CH<sub>4</sub> and CH<sub>4</sub>-CO<sub>2</sub> Mixtures. *J. Catal.* **2005**, *230*, 173–185.
- (23) Ding, W.; Li, S.; Meitzner, G. D.; Iglesia, E. Methane Conversion to Aromatics on Mo/H-ZSM5: Structure of Molybdenum Species in Working Catalysts. *J. Phys. Chem. B* **2001**, *105*, 506–513.
- (24) Li, B.; Li, S.; Li, N.; Chen, H.; Zhang, W.; Bao, X.; Lin, B. Structure and Acidity of Mo/ZSM-5 Synthesized by Solid State Reaction for Methane Dehydrogenation and Aromatization. *Micro-porous Mesoporous Mater.* **2006**, *88*, 244–253.
- (25) Liu, S.; Wang, L.; Ohnishi, R.; Ichikawa, M. Bifunctional Catalysis of Mo/HZSM-5 in the Dehydroaromatization of Methane to Benzene and Naphthalene XAFS/TG/DTA/ MASS/FTIR Characterization and Supporting Effects. *J. Catal.* **1999**, *181*, 175–188.
- (26) Borry, R. W., III; Kim, Y. H.; Huffsmith, A.; Reimer, J. A.; Iglesia, E. Structure and Density of Mo and Acid Sites in Mo-Exchanged H-ZSM5 Catalysts for Nonoxidative Methane Conversion. *J. Phys. Chem. B* **1999**, *103*, 5787–5796.
- (27) Solymosi, F.; Cserényi, J.; Szöke, A.; Bánsági, T.; Oszkó, A. Aromatization of Methane over Supported and Unsupported Mo-Based Catalysts. *J. Catal.* **1997**, *165*, 150–161.
- (28) Matus, E. V.; Ismagilov, I. Z.; Sukhova, O. B.; Zaikovskii, V. I.; Tsikoza, L. T.; Ismagilov, Z. R.; Moulijn, J. A. Study of Methane Dehydroaromatization on Impregnated Mo/ZSM-5 Catalysts and Characterization of Nanostructured Molybdenum Phases and Carbonaceous Deposits. *Ind. Eng. Chem. Res.* **2007**, *46*, 4063–4074.
- (29) Deaven, D. M.; Ho, K. M. Molecular Geometry Optimization with a Genetic Algorithm. *Phys. Rev. Lett.* **1995**, *75*, 288–291.
- (30) Holland, J. H. *Adaptation in Natural and Artificial Systems: An Introductory Analysis with Applications to Biology, Control, and Artificial Intelligence*; University of Michigan Press: Ann Arbor, MI, 1975.
- (31) Kabrede, H.; Hentschke, R. An Improved Genetic Algorithm for Global Optimization and Its Application to Sodium Chloride Clusters. *J. Phys. Chem. B* **2002**, *106*, 10089–10095.
- (32) Andre, J.; Siarry, P.; Dognon, T. An Improvement of the Standard Genetic Algorithm Fighting Premature Convergence in Continuous Optimization. *Adv. Eng. Softw.* **2001**, *32*, 49–60.
- (33) Woodley, S. M.; Catlow, C. R. A. Structure Prediction of Titania Phases: Implementation of Darwinian versus Lamarckian Concepts in an Evolutionary Algorithm. *Comput. Mater. Sci.* **2009**, *45*, 84–95.
- (34) Glazneva, T. S.; Kotsarenko, N. S.; Paukshtis, E. A. Surface Acidity and Basicity of Oxide Catalysts: From Aqueous Suspensions to In Situ Measurements. *Kinet. Catal.* **2008**, *49*, 859–867.
- (35) Vimont, A.; Thibault-Starzyk, F.; Lavalley, J. C. Infrared Spectroscopic Study of the Acidobasic Properties of Beta Zeolite. *J. Phys. Chem. B* **2000**, *104*, 286–291.
- (36) Tessonnier, J.-P.; Louis, B.; Rigolet, S.; Ledoux, M. J.; Pham-Huu, C. Methane Dehydro-Aromatization on Mo/ZSM-5: About the Hidden Role of Brønsted Acid Sites. *Appl. Catal., A* **2008**, *336*, 79–88.
- (37) Hanif, A.; Xiao, T.; York, A. P. E.; Sloan, J.; Green, M. L. H. Study on the Structure and Formation Mechanism of Molybdenum Carbides. *Chem. Mater.* **2002**, *14*, 1009–1015.
- (38) Nagai, M.; Nishibayashi, T.; Omi, S. Molybdenum Carbides and Carbonaceous Carbons on Mo/Al-FSM16 for Methane Conversion. *Appl. Catal., A* **2003**, *253*, 101–112.
- (39) Oshikawa, K.; Nagai, M.; Omi, S. Characterization of Molybdenum Carbides for Methane Reforming by TPR, XRD, and XPS. *J. Phys. Chem. B* **2001**, *105*, 9124–9131.
- (40) Dědeček, J.; Sobalík, Z.; Wichterlová, B. Siting and Distribution of Framework Aluminium Atoms in Silicon-Rich Zeolites and Impact on Catalysis. *Catal. Rev.—Sci. Eng.* **2012**, *54*, 135–223.

(41) Tessonnier, J.-P.; Louis, B.; Walspurger, S.; Sommer, J.; Ledoux, M.-J.; Pham-Huu, C. Quantitative Measurement of the Brønsted Acid Sites in Solid Acids: Toward a Single-Site Design of Mo-Modified ZSM-5 Zeolite. *J. Phys. Chem. B* **2006**, *110*, 10390–10395.

(42) Sklenak, S.; Dědeček, J.; Li, C.; Wichterlová, B.; Gábová, V.; Sierka, M.; Sauer, J. Aluminium Siting in the ZSM-5 Framework by Combination of High Resolution  $^{27}\text{Al}$  NMR and DFT/MM Calculations. *Phys. Chem. Chem. Phys.* **2009**, *11*, 1237–1247.

(43) Handzlik, J.; Ogonowski, J. Structure of Isolated Molybdenum-(VI) and Molybdenum(IV) Oxide Species on Silica: Periodic and Cluster DFT Studies. *J. Phys. Chem. C* **2012**, *116*, 5571–5584.